Earth and Planetary Science Letters 584 (2022) 117479

Contents lists available at ScienceDirect

Earth and Planetary Science Letters

www.elsevier.com/locate/epsl

Consistent detachment of supracrustal rocks from a fixed subduction depth in the Cyclades

Bertram Uunk [a,*], Fraukje Brouwer [a], Manuel de Paz-Álvarez [b], Kirsten van Zuilen [a], Rosanne Huybens [a], Reinier van 't Veer [a], Jan Wijbrans [a]

[a] Vrije Universiteit Amsterdam, De Boelelaan 1085, 1081HV Amsterdam, the Netherlands
[b] University of Oviedo, Calle Jesús Arias de Velasco, 33005 Oviedo, Asturias, Spain

ARTICLE INFO

Article history:
Received 7 December 2021
Received in revised form 25 February 2022
Accepted 28 February 2022
Available online 17 March 2022
Editor: R. Bendick

Keywords:
subduction zones
exhumation
high-pressure metamorphism
geochronology
Cycladic Blueschist Unit

ABSTRACT

While subduction zones recycle Earth's crust back into the mantle, high pressure metamorphic rocks exposed at the surface testify to occasional crustal subduction failure. Balancing the budget of Earth's recycling factory requires a fundamental comprehension of how and when some crustal rocks are returned to the surface. Here, we constrain the timing and conditions for rocks that were subducted, exhumed and now exposed on Syros and Sifnos islands (Cyclades, Greece). Detailed petrochronology on domains of supracrustal oceanic, passive margin and continental provenance shows that progressive subduction and exhumation has resulted in imbrication of a former continental margin. The consistency of age groups in 2–4 Myr intervals across two islands suggests episodic triggering of exhumation of coherent slices, similar to nappe stacking in the upper levels of orogens. Similar maximum burial conditions across the domains indicate that their highly variable material properties have not exerted a control on the depth from which they were recovered, and supracrustal exhumation was instead triggered by a steady state mechanism operating at ~65–70 km depth in the subduction zone. We propose that for mechanically strong rocks, consistent exhumation may have been triggered by thermal weakening at the depth of coupling between the subducting slab and mantle wedge corner flow in an extended back-arc. For weakly coupled supracrustal rocks, consistent exhumation may have been triggered by a stepped buoyancy increase for subducting rocks at the crust mantle boundary of a thickened overlying plate. These models help to understand the mechanisms and conditions by which supracrustal rocks may be systematically detached from a downgoing plate.

1. Introduction

Models for crustal accretion in subduction zones include exhumation through a subduction channel (Shreve and Cloos, 1986), underplating at the base of the upper plate (Platt, 1986) or relamination of melts or diapirs rising through the mantle wedge (Hacker et al., 2011). Crustal return may be driven by internal buoyancy forces (Ernst et al., 1997; Hacker et al., 2011) or external expulsion forces (Gerya et al., 2002; Warren et al., 2008). Rocks may exhume as a chaotic mélange (Shreve and Cloos, 1986) or as coherent units (Chemenda et al., 1996). All of these mechanisms require detachment of rocks from the subducting plate, inhibiting their further subduction and allowing exhumation. Understanding the mechanisms for rock detachment at mantle depths may help to establish the criteria by which crustal rocks fail to recycle into the mantle. Rocks exhumed at subduction zones may preserve crucial information as their maximum experienced pressure and temperature (P-T) reflect the circumstances at which they detached from the subducting plate. Comparing these maximum burial conditions for different rocks and over time may permit relating them to specific processes or subduction zone properties. If a process can be successfully correlated to trigger rock exhumation, criteria that determine rock recycling or recovery may be stipulated.

The Cycladic Blueschist Unit (CBU) in Greece exposes subducted and exhumed rocks that underwent Eocene high pressure metamorphism (van Hinsbergen et al., 2005). Despite being a well-studied subduction complex, its internal structure and coherence during subduction and exhumation is debated. Some authors argue that Cycladic islands either belong to an imbricated lower or upper Cycladic nappe (Grasemann et al., 2017), and that P-T-t histories are homogeneous at the island-scale (Keiter et al., 2011). Others argue that islands expose stacked tectonic slices that can be correlated across islands (Forster and Lister, 2005;

* Corresponding author.
E-mail address: b.a.uunk@vu.nl (B. Uunk).

https://doi.org/10.1016/j.epsl.2022.117479

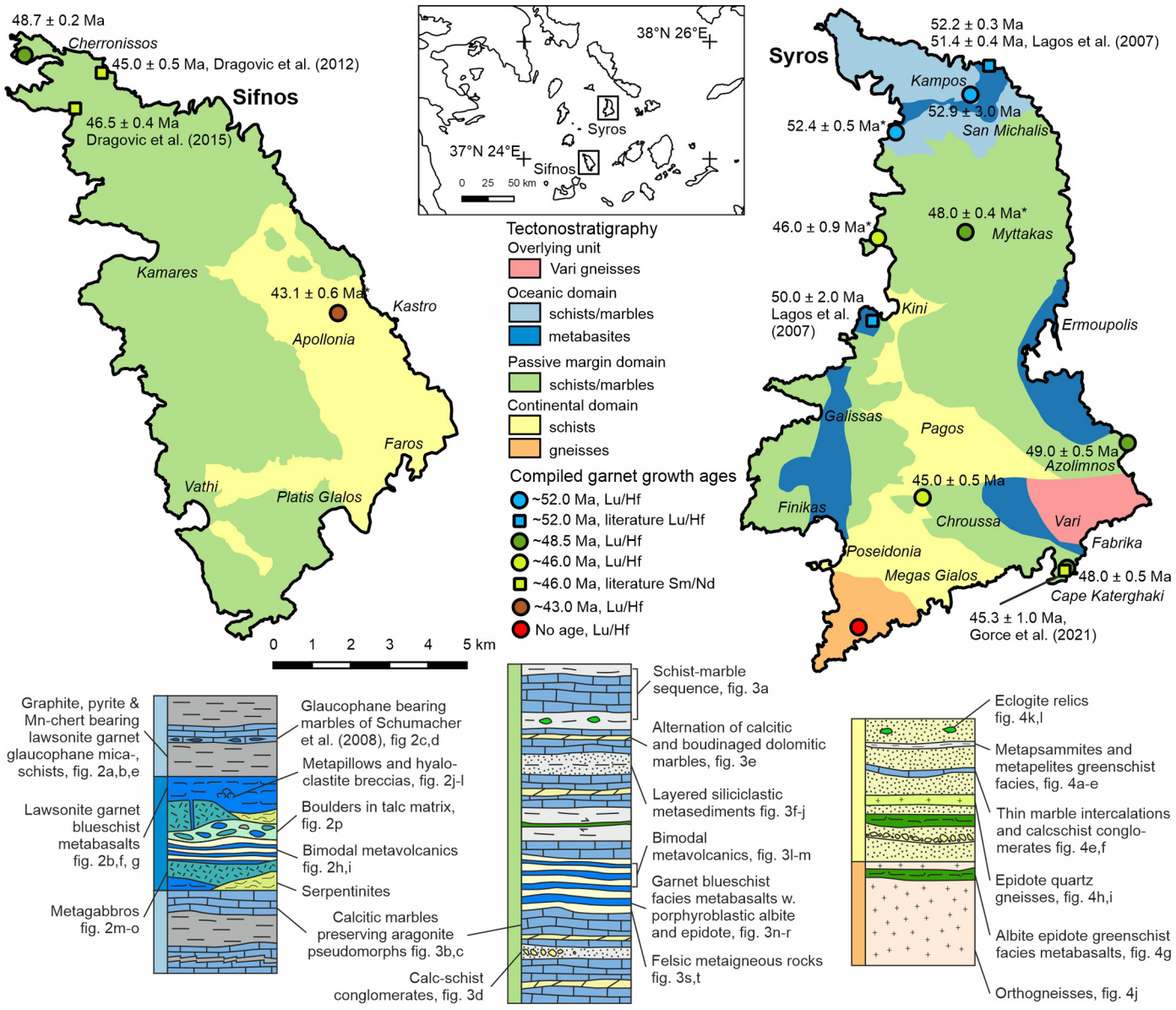

Fig. 1. Mapped domains of interpreted oceanic (dark/light blue), passive (green) and continental (yellow/orange) lithologies on Syros and Sifnos (top) and schematic stratigraphic columns for the oceanic domain (bottom left), passive margin domain (bottom center) and continental domain (bottom right). Compiled Lu/Hf and Sm/Nd garnet ages are indicated on the maps, ages marked with an asterisk reflect samples selected for thermodynamic modelling. (For interpretation of the colors in the figure(s), the reader is referred to the web version of this article.)

Glodny and Ring, 2021) and that metamorphic timing and conditions vary on the island-scale (Trotet et al., 2001). Our study focuses on the islands of Syros and Sifnos, where varying garnet growth ages for oceanic rocks (52 Ma; Lu/Hf from Lagos et al., 2007) and metavolcanic rocks (45–46 Ma; Sm/Nd from Dragovic et al., 2012, 2015; Gorce et al., 2021) suggest metamorphism is not homogeneous across the sequence. Contrasting structural interpretations for these islands have spawned multiple geologic maps, where authors divide the CBU in varying lithologically heterogenous subunits and lay emphasis on different tectonic contacts (Avigad, 1993; Aravadinou et al., 2015; Laurent et al., 2016; Philippon et al., 2011; Roche et al., 2016). Others draw a strictly lithology based map and interpret islands to reflect a single tectonic unit (Keiter et al., 2011).

Based on field observations and published maps (Keiter et al., 2011; Laurent et al., 2016; Philippon et al., 2011; Roche et al., 2016), we take an alternative approach of subdividing the sequence in domains of interpreted provenance (Fig. 1). We define an uppermost oceanic domain, and intermediate passive margin domain and a lowermost continental domain, reflecting a more distal or proximal continental margin provenance. We show that our subdivision of suites of lithologies correlates to differences in preservation of HP/LT assemblages (Figs. 2–4). To constrain subduction ages for the sequence, ten samples from all domains were selected for garnet-whole rock Lu/Hf dating (Fig. 1). For each of the domains, we constrain the P-T conditions of garnet growth using thermodynamic modelling. We show that the islands consist of imbricated subunits that were subducted and exhumed at ∼ 2–4 Myr intervals during the transition from oceanic to continental subduction. The different subunits record similar maximum burial conditions, indicating a common mechanism has triggered their subsequent exhumation. Due to their varying provenance and thus material properties, we interpret the common exhumation mechanisms to relate to steady state properties of the subduction zone. We propose that recurrent rock exhumation may either be triggered by thermal weakening at the depth at which mantle wedge corner

Fig. 2. Field photographs displaying typical lithologies mapped as having an oceanic provenance. a) Graphitic metasediments preserving mm-sized garnet and cm-sized lawsonite pseudomorphs, viewed on the foliation plane. b) Comparison of gray, graphite-bearing lawsonite pseudomorphs in a calcschist (in front) with white lawsonite pseudomorphs in a metabasaltic blueschist (in the back). c, d) Eclogitic metabasalt boudins in mylonitic impure marbles. e) Polyphase-folded Mn-chert layer in graphite schists. f) Blueschist facies metabasalt with omphacitite clasts. g) Blueschist facies metabasalt showing porphyroblastic lawsonite. h, i) Bimodal metavolcanics with garnet blueschist facies mineralogy showing crenulation folding (h) and horizontal compositional layering (i). j) Garnet-glaucophanite lenses with fine-grained margins in micaschists, representing possible metapillows and interstitial sediments. k) Undeformed hyaloclastite breccia with a garnet blueschist facies assemblage, field of view is $\sim$ 20 m. l) Boulder in hyaloclastite breccia, showing fine-grained chilled margins transformed by blueschist facies metamorphism. m) Glaucophane-eclogite metagabbro cross-cut by garnet-blueschist metadolerite. n) Slightly deformed glaucophane + zoisite + phengite metagabbro crosscut by eclogite facies metadolerite dyke. o) Omphacite-zoisite metagabbro. p) Mélange of $<$ 2 m meta-igneous boulders in talc schist matrix. (For high resolution version of the images, the reader is referred to the web version of this article.)

flow couples to the subducting slab, or by a stepped increase in subducting rock buoyancy at the crust mantle boundary in the overlying plate. Both may provide mechanisms for the observed systematic detachment behavior for supracrustal rocks from a continuously downgoing plate during the transition of oceanic to continental subduction.

2. Distal to proximal shelf lithologies

2.1. Oceanic domain

The top of the CBU consists of an oceanic domain of siliciclastic metasediments with subordinate marbles (Fig. 2a–e), as well as a mafic-ultramafic meta-igneous suite (Fig. 2f–p), all preserving blueschist and eclogite facies mineral assemblages. Oceanic metasedimentary lithologies are variably calcitic metapelites tectonically intercalated by metabasaltic glaucophanites or metagabbros, which all locally contain porphyroblastic garnet and lawsonite (Hamelin et al., 2018; Philippon et al., 2013), but lack porphyroblastic epidote. Pure calcite marbles preserve columnar calcite resulting from topotactic replacement of aragonite (Brady et al., 2004) and range to strongly impure marbles containing glaucophane, Na-pyroxene, epidote, garnet and/or white mica (Schumacher et al., 2008). Mafic minerals occur as boudins and as isolated crystals floating in a calcite marble matrix (Fig. 2c, d). Mafic silicate minerals in marbles are exclusive to the oceanic domain,

Fig. 3. Field photographs displaying typical lithologies mapped as having a passive margin provenance. a) Intercalated gray marbles and siliciclastic lithologies overgrown by vegetation. b) Subvertical calcite lineation defined by columnar pseudomorphs after aragonite in a graphite-rich marble, intercalated by chert layers. c) Subvertical columnar calcite after aragonite, which has overgrown isoclinal recumbent folding. d) Calc-schist conglomerates. e) Interlayered gray calcitic and white/yellow boudinaged dolomitic marbles. f) Psammitic metasediments displaying apparent rhythmic layering. g) Alternation of garnet-bearing and glaucophane-bearing pelitic micaschists. h) Quartz-calcschists, showing isoclinal recumbent folding. i) Folded quartzite statically overgrown by semi-skeletal garnet. j) Isoclinally folded Mn-chert layers between mafic metavolcanics. l) Outcrop of a layered metavolcanic sequence. k) Bimodal metavolcanics with garnet blueschist facies mineralogy. i) Bimodal mafic blueschist and felsic metavolcanics. n, o) Porphyroblastic epidote, garnet and paragonite in different sizes in a blueschist, forming a typical assemblage for the passive margin domain. p) Intermediate composition metavolcanic rock with an eclogite facies assemblage of white mica, garnet and bright green omphacite at the location of sample F11.08b. q) Coarse-grained garnet-epidote-glaucophane metavolcanic rock. r) Folding in layered metavolcanics expressed by variable proportions of omphacite, glaucophane, epidote and ankerite. Width of view 25 cm. s) Quartz-jadeite gneiss with porphyroblastic garnet and glaucophane. t) Centimeter-sized garnet in a quartz-feldspar orthogneiss. (For high resolution version of the images, the reader is referred to the web version of this article.)

Fig. 4. Field photographs displaying typical lithologies mapped as have a continental provenance. a) Layered greenschist facies metapsammites. b) Quartz-epidote-albite metapsammite showing recumbent folding. c) Layered metapsammites and metapelites, preserving chloritized garnets. d) Crenulated pelitic schist with folded quartz lenses. e) Thin marble intercalation in greenschist facies metapsammites. f) Calc-schist conglomerate, calcite in calcite pebbles in granoblastic. g) Albite-chlorite greenschist facies metabasalt. h, i) Folded quartz-epidote gneiss. j) Layered dacitic orthogneisses. k, l) Fractured mafic eclogite relic in layered metapsammites (l is a detail of k). (For high resolution version of the images, the reader is referred to the web version of this article.)

where silicate minerals in marbles in other domains are limited to white mica and quartz, with rare epidote and garnet. An oceanic crustal provenance for the metasediments is interpreted based on Mn-chert layers (Fig. 2e) interpreted to reflect seafloor hydrothermal activity (Keiter et al., 2011) and by graphite (Fig. 2a, e) and pyrite, indicating anoxic, probably deep sea depositional conditions. Lawsonite bearing graphitic schists, with or without pyrite and Mn-chert are diagnostic for metasediments of the oceanic domain.

The mafic-ultramafic meta-igneous suite is interpreted as former oceanic crust formed in a back-arc setting (Seck, 1996). The suite consists of hectometer sized metavolcanic (Fig. 2f–l) or metagabbroic bodies (Fig. 2m–o) as well as up to 100-meter-thick mélange zones (Fig. 2p), containing deci- to decameter sized heterogeneous boulders in a chlorite-talc schist or serpentinite matrix. Boulders and larger bodies preserve eclogite and lawsonite blueschist facies assemblages, consisting of mostly omphacite, glaucophane, garnet and minor epidote. Larger meta-igneous bodies include variably deformed metabasalts (Fig. 2f, g), bimodal metavolcanics (Fig. 2h, i), volcanic agglomerates and hyaloclastite breccias (Fig. 2j–l) and metagabbros (Fig. 2m–o), which all locally preserve primary magmatic textures. Mafic rocks of the oceanic domain can be distinguished from other mafic suites in the CBU by the preservation of lawsonite pseudomorphs, the absence of porphyroblastic epidote and the presence of ultramafic talcschists and serpentinites with metasomatized boulders (Fig. 2p) or $>$ 100 m thick bodies of metagabbro or metabasalt, which are exclusive to this domain.

While oceanic metasediments only occur in north Syros, oceanic metabasites also occur in south Syros near the towns of Kini, Ermoupolis and between Finikas and Galissas (Fig. 1). Most other authors map a similar distribution for oceanic metabasites (Keiter et al., 2011; Laurent et al., 2016; Philippon et al., 2011). Our mapping of the domain of oceanic provenance also includes the schists and marbles directly above and below the metabasites in north Syros. We do this because 1) depositional characteristics indicate a deep-sea setting and hydrothermal alteration (Fig. 2a, e), consistent with sediments belonging to oceanic crust, 2) smaller volumes of oceanic-type metabasalts and metagabbros occur in the metasedimentary schists (Fig. 2c, d; Keiter et al., 2011), and 3) the sediments show similar preservation of lawsonite-bearing high-pressure metamorphic assemblages to the metabasites (Fig. 2a, b, g; Philippon et al., 2013), indicating they may have formed a composite tectonic unit during their metamorphic history.

2.2. Passive margin domain

The tectonostratigraphically intermediate passive margin domain is dominated by marbles (Fig. 3a–e), intercalated with siliciclastic metasediments (Fig. 3f–j), as well as with felsic, intermediate and mafic metavolcanics (Fig. 3l–t). This domain is interpreted as a volcano-sedimentary sequence associated with an

extended continental shelf (Keiter et al., 2011; Ring et al., 2020). Most siliciclastic lithologies preserve a garnet-blueschist facies foliation, which is statically overgrown by porphyroblastic epidote and/or paragonite (Fig. 3g, k, n–s). Replacement of glaucophane and garnet with chlorite and/or albite indicates static greenschist overprinting. Dynamic greenschist overprint is limited to meter-scale chlorite-bearing shear zones.

Marbles preserve columnar calcite habits after aragonite replacement (Fig. 3b, c), similar to the oceanic domain. Calcitic lithologies also include calc-schist conglomerates (Fig. 3d). Typical to marbles in the passive margin is that they are intercalated with boudinaged dolomitic marbles (Fig. 3e; Philippon et al., 2011; Schumacher et al., 2008). Impure marbles in the passive margin domain contain white mica, quartz and minor garnet or epidote. Siliciclastic metasediments include interlayered metapsammites and metapelites (Fig. 3f, g) quartz-calcschists (Fig. 3h) and quartzites (Fig. 3i), which may contain conglomeratic levels. Locally, Mn-chert layers (Fig. 3j) indicate deep water conditions. Layered bimodal metavolcanics (Fig. 3l–m) are interpreted to reflect rift related volcanism (Pe-Piper, 1998). Metavolcanics also include more basaltic to intermediate compositions (Fig. 3n–r) and felsic gneisses (Fig. 3s, t).

The passive margin domain covers most of the central and northern parts of both Syros and Sifnos. While most authors map the Eclogite-Blueschist Unit (EBU) on Sifnos tectonically separate (Aravadinou et al., 2015; Avigad, 1993; Roche et al., 2016), we include the sequence of metavolcanics and subordinate marbles in north Sifnos in the passive margin domain. We do so because 1) similar metavolcanics and metasediments also occur in smaller schist lenses between marbles on Syros and Sifnos (Fig. 3l–m), 2) the rocks similarly preserve blueschist facies assemblages with porphyroblastic epidote and paragonite (Fig. 3n–r), and 3) the association of marbles and bimodal volcanics fits a rifted continental margin provenance (Pe-Piper, 1998; Ring et al., 2020). On Syros, similar EBU-type rocks occur in the coastal sections between Delfini and Kini and between Fabrikas and Cape Katerghaki. Some previous authors map this latter sequence as belonging to oceanic metabasites (Keiter et al., 2011; Laurent et al., 2016). We incorporate it in the passive margin domain due to the abundance of porphyroblastic epidote and the absence of ultramafic rocks and lawsonite pseudomorphs. The passive margin domain also includes the 'Syringas marker succession' identified by Keiter et al. (2011).

2.3. Continental domain

The lowermost, continental domain consists of siliciclastic metasediments (Fig. 4a–d), intercalated with thin marble layers (Fig. 4e, f), mafic metavolcanics (Fig. 4g) and gneisses (Fig. 4h–j), interpreted as continental basement and associated sedimentary cover. Most lithologies are pervasively overprinted by greenschist facies metamorphism. Where blueschist facies textures are preserved, garnet and glaucophane are commonly statically chloritized. Rare eclogitic relics in both the gneisses and metasediments (Fig. 4k, l) provide field evidence for high pressure metamorphism for this domain (Keiter et al., 2011; Laurent et al., 2016; Roche et al., 2016). The absence of $>$ 50 m thick marble layers, the presence of $>$ 50 m thick gneiss sequences and the dominance of pervasively overprinted greenschist facies mineral assemblages are diagnostic for the continental domain.

Continental metasediments are commonly metapsammites (Fig. 4a, b) and metapelites (Fig. 4b–d). Minor marble or calc-schist conglomerate intercalations are up to 50 m thick (Fig. 4e, f). Preservation of columnar aragonite pseudomorphs has not been identified: calcite is granoblastic (Fig. 4f). Mafic metabasalts occur in both the sedimentary sequence as well as in the basement gneisses (Fig. 4g). Quartz-epidote gneisses occur in the metasedimentary sequence (Fig. 4h, i), crosscut by calcite and/or epidote veins. Greenschist facies assemblages typically include epidote, chlorite, albite and locally biotite or actinolite (Fig. 4g–i). Paragneisses and orthogneisses (Fig. 4j) with K-feldspar augen represent a Variscan basement (Keiter et al., 2011).

The continental domain covers southern parts of Syros and Sifnos. Previous authors include the schist and marble sequence between Galissas and Pagos in South central syros in the greenschist facies overprinted basement units (Laurent et al., 2016). We map this area as the passive margin unit as it exposes lithologies with a passive margin provenance preserving blueschist facies assemblages and is distinctly different from the siliciclastic metasediments with greenschist facies assemblages of the continental domain. This interpretation is further supported by occurrences of the 'Syringas marker succession' in these areas (Keiter et al., 2011), which are interpreted to belong in the passive margin domain.

3. Sample petrography and garnet mineral chemistry

Sample locations are plotted in Fig. 1 and given as GPS coordinates in Table S1. Fig. 5 shows sample and garnet petrography, as well as core to rim garnet mineral chemistry.

3.1. Oceanic domain

Sample 16SR09 is a glaucophane garnet lawsonite titanite calcschist collected along the coast west of San Michalis, Syros. Blueschist foliation postdates euhedral garnet, which contain abundant quartz inclusions. Garnet and glaucophane are locally retrogressed to chlorite. Sample SY17-30 is glaucophane garnet titanite quartz micaschist collected just above the metabasites near Kampos, Syros. Blueschist foliation postdates euhedral garnets, which is retrogressed along grain boundaries and in cracks to biotite. Garnet is inclusion-poor, including quartz, mica and titanite.

3.2. Passive margin domain

Sample 17SI06c is a glaucophane eclogite collected north of Cheronissos, Sifnos. Porhyroblastic glaucophane and garnet have overgrown an omphacite, epidote and phengite foliation. Garnet is euhedral, unretrogressed and contains inclusions of epidote and omphacite. Sample 12SR18b is garnet epidote blueschist collected west of Myttakas, Syros. Garnet predates a glaucophane, phengite, quartz and epidote foliation, which is overgrown by porphyroblastic albite. Glaucophane and garnet are statically retrogressed to chlorite.

Sample F11.08b is an eclogite collected near Katerghaki Cape, south Syros. Euhedral garnet has overgrown an omphacite, epidote and phengite texture. Garnet is unretrogressed and contains inclusions of omphacite and epidote. Sample H8.09 is an eclogite collected on the coast north of Azolimnos, Syros. Garnet has statically overgrown an omphacite, phengite and epidote foliation. Omphacite has retrogressed to glaucophane. Spiraling inclusion trails indicating syntectonic garnet growth.

Sample 17SR21 is a garnet glaucophane micaschist collected along the coast northwest of Kini, Syros. Euhedral garnet predates a phengite, glaucophane and quartz foliation. Garnet is locally statically retrogressed to chlorite. Albite has overgrown the blueschist foliation. Garnet is inclusion-poor, including only quartz. Sample C405 is an eclogite collected west of Chroussa, Syros. Garnet has overgrown an omphacite, epidote, quartz and phengite foliation and contains abundant inclusions of matrix minerals. Garnet pressure shadows contain glaucophane and phengite.

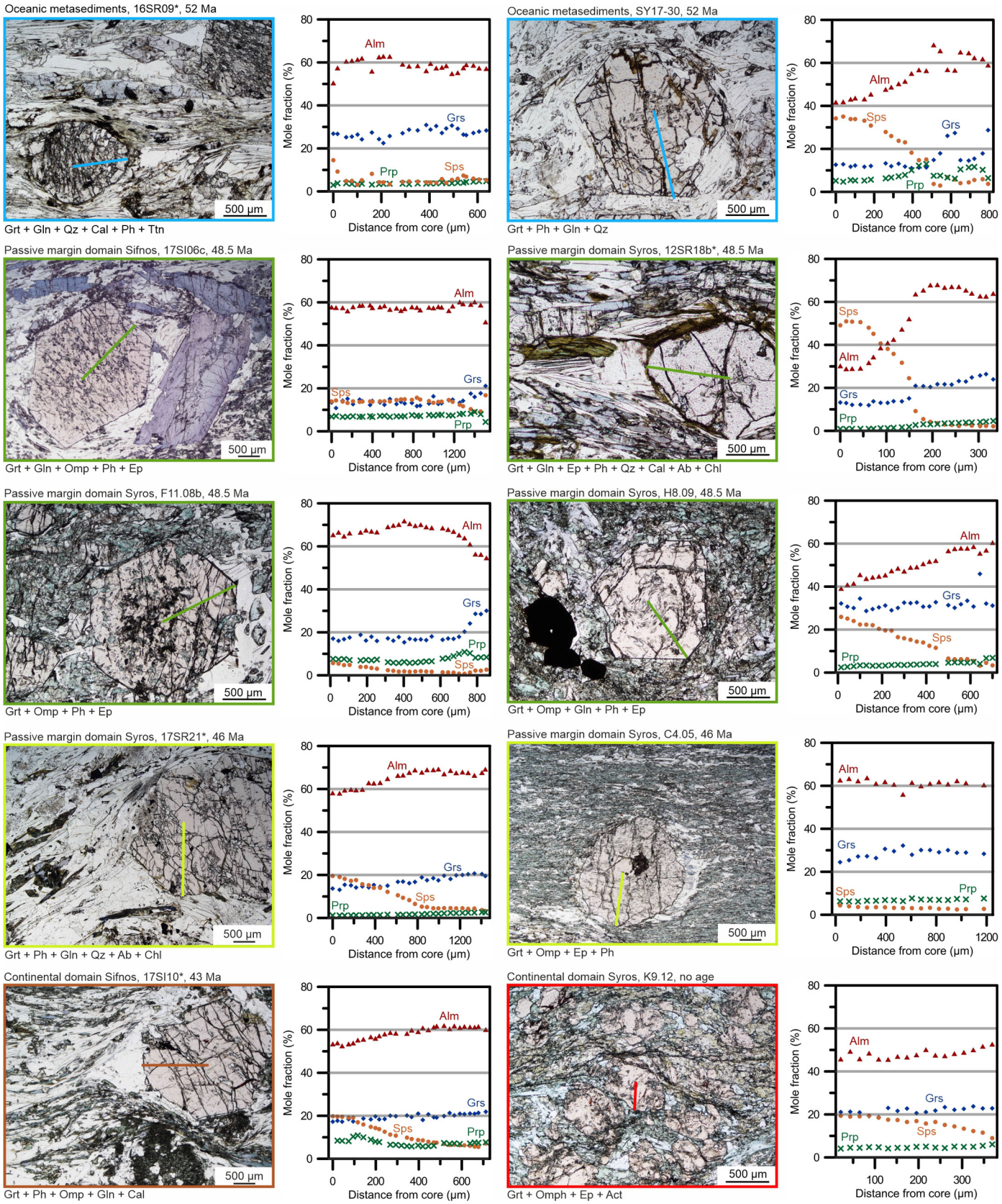

Fig. 5. Garnet petrography and major element geochemistry. Frame color reflects the sample's respective Lu/Hf age group, corresponding to Fig. 1. Mole fractions indicated for garnet compositions: Almandine (Alm), pyrope (Prp), grossular (Grs) and spessartine (Sps). Samples indicated by an asterisk were selected for thermodynamic modelling.

3.3. Continental domain

Rare preservation of fresh garnet has strongly limited the sampleset for the continental domain. Sample K9.12 is a statically retrogressed eclogite collected south of Posidonia, Syros. Relic, irregular garnet occurs between a statically retrogressed matrix of actinolite replacing omphacite and epidote. Garnet has irregular boundaries and is relatively inclusion free. Sample 17SI10 is an eclogitic micaschist collected along the road between Apollonia and Kastro, Sifnos. Garnet predates an omphacite, phengite and epidote foliation, where omphacite is statically retrogressed to glaucophane. Euhedral garnet is relatively inclusion free, locally retrogressed to chlorite and albite.

3.4. Garnet chemistry

Garnet compositions were analyzed in polished thin sections using wavelength dispersive spectrometry on the JEOL JXA-8530F Hyperprobe electron probe micro-analyzer hosted by Utrecht University. Acceleration voltage was 15 kV with a probe current of 15 or 20 nA, using a beam size of 1 or 3 µm. Measurements were calibrated to natural mineral standards. Results for garnet EPMA analysis are given in Table S2. Garnet is generally almandine-rich (Fig. 5), ranging between 55–70% at garnet rims. Spessartine contents for the core show variation from up to ~ 50% (12SR18b), to hardly any enrichment at 5% (C4.05). Pyrope contents range between 0 to 10% and grossular ranges between 10 to 30%. Garnet chemistry for samples 12SR18b, H8.09, 17SR21, 17SI10 and K9.12 show relatively simple compositional zoning patterns, including a gradual decrease in spessartine and an increase of grossular, pyrope and especially almandine contents towards the rims, indicative of growth along a prograde P-T path (Tracy et al., 1976). Samples C4.05, 17SI06c and 16SR09 display no significant zoning or a weakly developed similar trend. Sample SY17-30 and F11.0b show similar initial overall zoning patterns, where SY17-30 shows significant steps in the rim section indicative of a more complex growth and resorption history and F11.08b shows a rim-ward decrease in almandine and an increase in grossular.

4. Garnet – whole rock Lu/Hf dating

4.1. Methods

Garnet was separated from the 250–500 µm fraction of crushed sample using heavy-liquid density and magnetic separation. Separates were crushed again in a steel mini-jaw crusher and sieved to 90–180 µm to expose mineral inclusions. As initially the study was intended to include Sm/Nd ages, a stepwise dissolution strategy was followed modified from Dragovic et al. (2015), followed by digestion on the hotplate following Lagos et al. (2007). Stepwise dissolution approaches have been hypothesized to potentially fractionate Lu/Hf during leaching (Scherer et al., 2000), but this is not indicated in our data set. The detailed procedure and the possibility for fractionation is discussed in Supplementary Text S1.

After digestion, lutetium and hafnium were chromatographically separated using Eichrom® Ln-spec resin following Münker et al. (2001). Both fractions were measured in low resolution mode using a ThermoFisher Neptune Plus MC-ICP-MS at VU Amsterdam. Hafnium fractions were dissolved to a 50 ppb Hf concentration in 0.56N HNO_3/0.24N HF and lutetium fractions to a maximum concentration of 20 ppb Lu in 1% HNO3. Data acquisition consisted of 50 cycles for Hf and 25 cycles for Lu, with an integration time of 4 s. Data were corrected for Yb interferences and instrumental mass bias following Vervoort et al. (2004).

A 50 ppb JMC-475 solution, one in-house standard for hafnium and one in-house standard for lutetium were measured multiple times during each analytical session to monitor instrumental precision. For the hafnium JMC-475 standard, long-term (3 yrs) $^{176}Hf/^{177}Hf$ values are 0.282160 ± 0.00019 (2sd). Blanks for the garnet stepwise dissolution and digestion procedure yielded values of 3.4, 3.8 and 22.7 pg for Lu and 6.8, 4.8 and 13.7 pg for Hf, respectively. Blank values for the digestion and separation procedure yielded values of 3.1 and 3.8 pg for Lu and 4.8 and 10.2 pg for Hf, respectively. Four analyses of powdered BHVO-2 rock standard included in the series yielded an average Lu concentration of 0.2814 ± 0.0020, an average Hf concentration of 4.500 ± 0.051 and a $^{176}Hf/^{177}Hf$ ratio of 0.283082 ± 0.000010 (all uncertainties as 2sd).

4.2. Isochron calculation, error propagation and outlier treatment

Results for Lu and Hf isotopic analysis are provided in Table S3. Garnet-whole rock Lu/Hf isochrons calculated using Isoplot 3.75 are shown in Fig. 6. For all isochrons, 2SE on individual isotope ratio analyses that were smaller than the long-term external precision of the isotope ratio of the primary JMC standard (0.000019, 2sd), were replaced by the latter. For samples 17SR21 and 17SI10, this procedure resulted in MSWD values of 0.15 & 0.16 respectively (gray shaded values in Fig. 6g, i), indicating significant overestimation of analytical uncertainty. For these samples, all analyses were done in one sequence and none of the data points were treated as outliers. Isochrons using the internal 2SE were also calculated, resulting in increased MSWD values of 0.41 & 0.51 respectively, while lowering errors on the isochron age (Fig. 6g, i).

For the other samples, seven out of 71 data points were omitted from isochron calculation. For samples 17SI06c, 12SR18b, F11.08b and 16SR09, whole rock – outlier isochrons result in ages up to ~ 5 Myr older than the isochron age (Fig. 6b–e). Zoned Sm/Nd geochronology on garnet from Syros and Sifnos has resolved older core ages (Dragovic et al., 2015; Gorce et al., 2021). Our stepwise dissolution techniques may have preferentially removed younger garnet rims, enriching the fractions in older garnet cores prior to dissolution. Alternatively, these fractions may be the result of incongruent dissolution during the stepwise digestion. Longer HF treatment would result in more precipitation of secondary fluorides, increasing the possibility that these fluorides are not fully removed during stepwise dissolution steps. In any case, we reject these outliers from isochron calculation, as we are interested in the bulk of garnet growth at peak metamorphism. One remaining garnet outlier for sample 16SR09 plots significantly away from the isochron, producing a WR-outlier isochron age of 103 ± 29 Ma (MSWD 446, Table S2). This outlier is interpreted the result of spike-sample disequilibrium or incongruent dissolution.

For one sample from the continental basement of Syros (K9.12), an isochron of all but one data points yields an age of 25.6 Ma ± 3.7 Ma with a high MSWD of 10.6 (Fig. 6j), significantly younger than other garnet growth ages ranging 52–43 Ma (this study; Dragovic et al., 2012, 2015; Gorce et al., 2021; Lagos et al., 2007). This age and scatter is most likely to be caused by analytical problems, such as spike-sample disequilibrium or fractionation during the stepwise dissolution techniques. An alternative, geologic interpretation could be that the garnet contains growth zones or crystal populations of significantly (> 20 Myr) differing ages. Garnet was recently modelled to have grown during Miocene Barrovian overprint in the metamorphic core of Naxos (Lamont et al., 2019). If this also occurred in the overprinted basement units of Syros, age populations of Eocene eclogitic garnet (e.g. ~ 44 Ma, upper gray line in Fig. 6j) and Miocene greenschist facies garnet growth (e.g. ~ 23 Ma, lower gray line in Fig. 6j) may be present in the samples. Variable mixing of these age components could lead to scatter between two endmember isochrons as in Fig. 6j. In any case, data from sample K9.12 cannot be used to date peak burial of the continental domain on Syros.

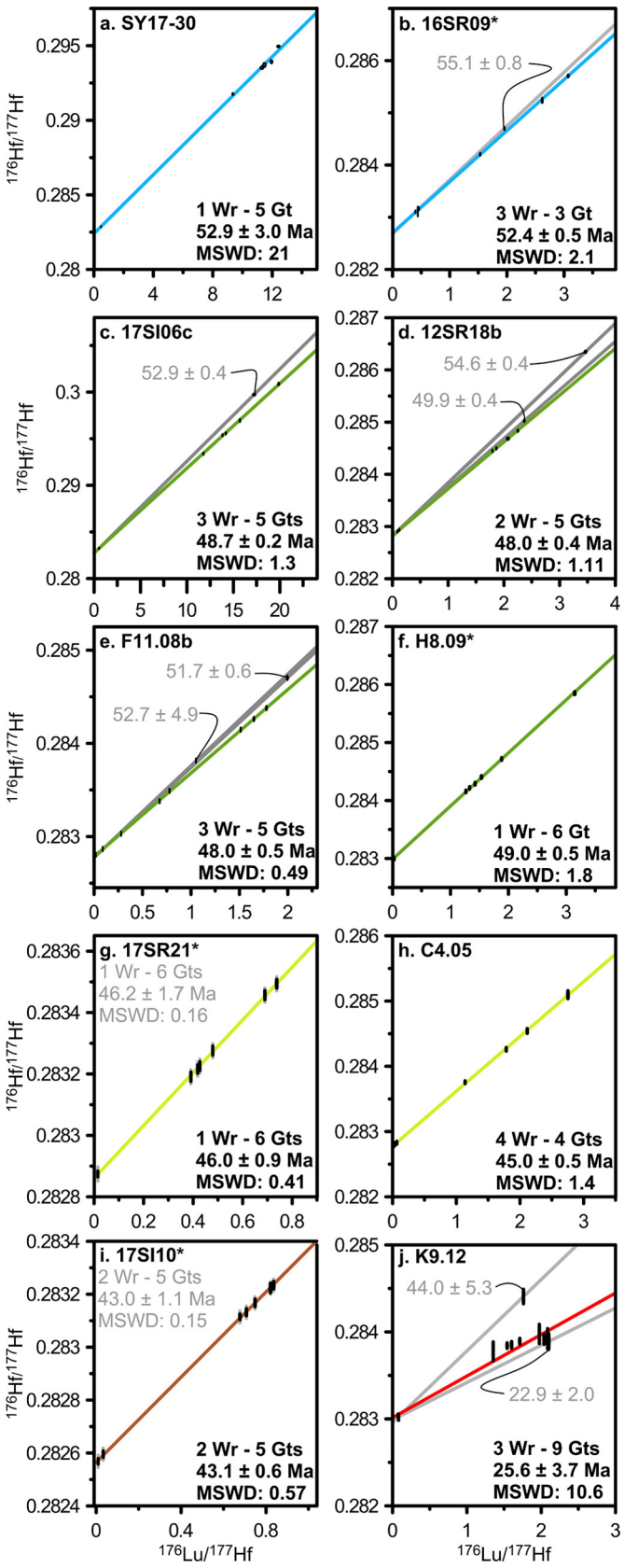

Fig. 6. Lu/Hf isochrons. Data points for garnet and whole rock analyses are plotted as 2sd error ellipses. Isochron ages for whole rock data and outlier garnet fractions are indicated near the garnet points. The accepted isochron ages for multiple garnet fractions are indicated in the bottom right of each panel. Samples indicated by an asterisk were selected for thermodynamic modelling.

Sample SY17-30 of the oceanic sediments yields a high MSWD of 21. EPMA garnet data for this sample (Fig. 5) shows complex major element zoning patterns interpreted to reflect growth and resorption alternations during metamorphism, which could cause a high MSWD due to age zonation. However, the age of oceanic domain doesn't depend on this sample, as oceanic metasediment sample 16SR09 was more successfully dated to 52.4 ± 0.5 Ma (Fig. 6b). Except for the sample SY17-30 and K9.12, all isochrons (Fig. 6) were constructed using six to eight data points, with MSWD values between 0.41 and 2.1. These MSWD values indicate any remaining geologic scatter does not significantly exceed our analytical uncertainty.

5. Thermodynamic modelling

For each of the domains, garnet core and rim growth was thermodynamically modelled using Perple_X 6.8.5 (Connolly, 2009), following Dragovic et al. (2012). Samples 16SR09 for the oceanic domain, 12SR18b and 17SR21 for the passive margin domain and 17SI10 from the continental domain were selected as garnet for these samples is euhedral with continuous compositional zoning patterns (Fig. 5), indicating that all compositional information was retained during exhumation. The data was supplemented with literature P-T conditions for garnet growth in oceanic metabasites (Laurent et al., 2018; Philippon et al., 2013) and for the passive margin domain of Sifnos (Dragovic et al., 2012). Garnet growth P-T estimates were modelled using the ds5.5 database and updates (Holland and Powell, 1998; hp62ver.dat). Solution models were used for garnet, biotite, chlorite, chloritoid (White et al., 2014), clinopyroxene (Green et al., 2007), feldspar (Fuhrman and Lindsley, 1988), clino-amphibole (Diener and Powell, 2012), epidote (Holland and Powell, 1998) and white mica (Smye et al., 2010). Garnet cores were modelled using bulk rock compositions and garnet rims were modelled using a calculated matrix composition following Dragovic et al. (2012). Major element bulk rock compositions (Table S4) were determined on fused glass beads using Philips Panalytical MagiXPro X-Ray Fluorescence spectrometer at VU Amsterdam, using an acceleration voltage of 40 kV and a beam current of 90 mA. Matrix compositions (Table S4) were calculated by substracting a volumetrically averaged garnet composition from the bulk chemistry, based on estimated garnet modal abundance from thin section and the density values as derived from Perple_X. Ferric iron contents were estimated based on the modal abundance and composition of ferric iron-bearing phases as determined by EPMA analysis. Pseudosections including modelled garnet modal abundances contours were constructed for samples 16SR09 and 12SR18b (Fig. 7) and samples 17SR21 and 17SI10 (Fig. 8). Conditions for garnet core and rim growth are plotted in the pseudosections based on intersection of almandine, spessartine and grossular isopleths following Dragovic et al. (2012). Pyrope isopleths were not used due to low contents ($X_{py} < 0.08$, Fig. 5) in the garnets.

6. Sequential subduction and exhumation of crustal slices

6.1. The age and conditions for maximum burial

Combining available Lu/Hf and Sm/Nd datasets reveals four age clusters (Fig. 9a). Five samples from the oceanic domain show overlapping ages averaging 52.0 ± 0.6 Ma. Eight samples from the passive margin domain form two age groups, averaging 48.6 ± 0.6 Ma and 45.8 ± 1.0 Ma respectively. One sample from the continental domain on Sifnos provided an age of 43.1 Ma ± 0.6 Ma. P-T conditions for garnet core and rim growth for the different age groups define a narrow range of 19–22 kbar and 450–550 °C (Fig. 9b). The peak temperature for all domains is below the estimated closure temperature of > 600 °C for the

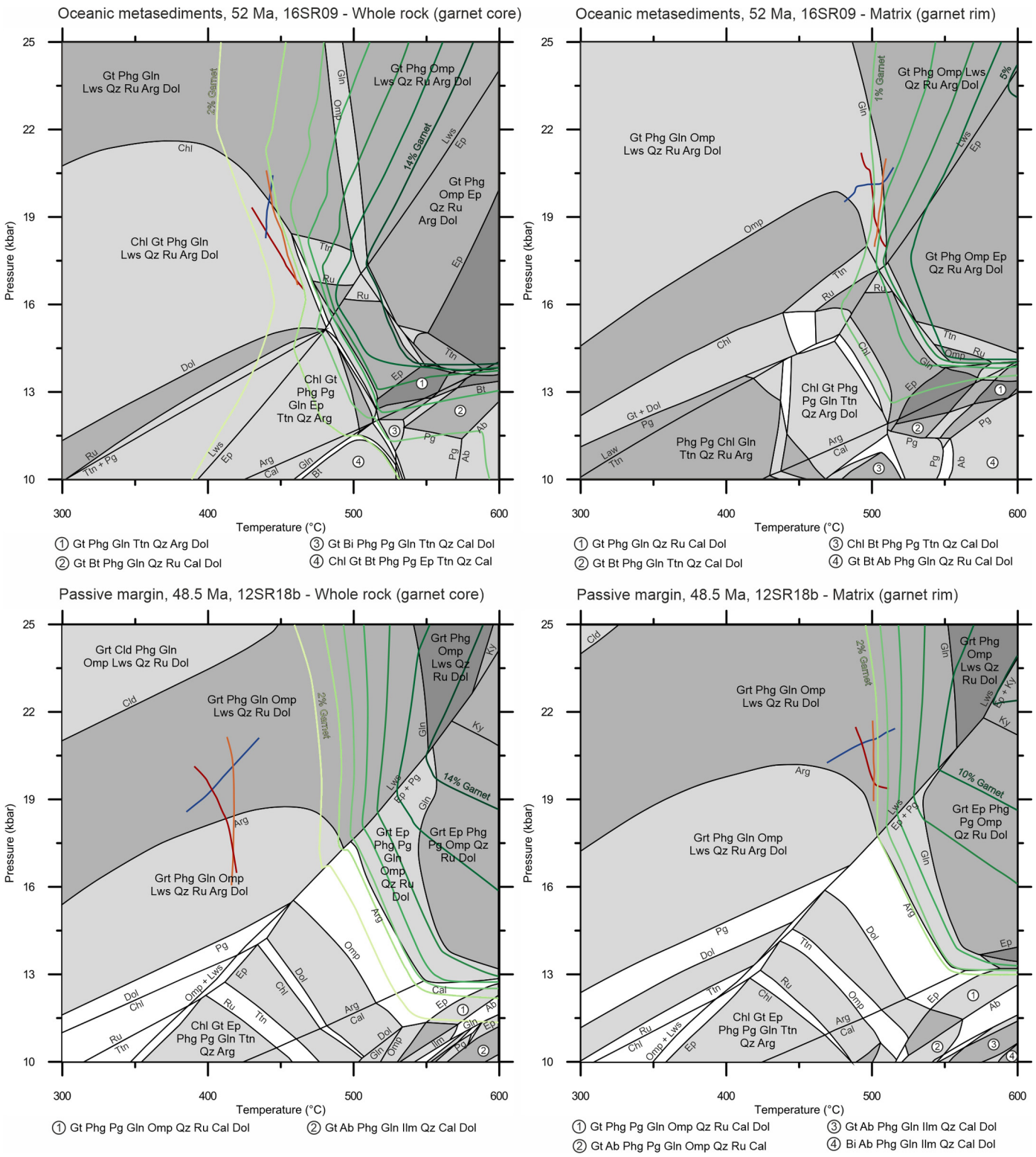

Fig. 7. Pseudosections for samples 16SR09 and 12SR18b. Models for whole rock and matrix compositions reflect respective garnet core and rim growth for the metasediments of the oceanic domain (16SR09) and the upper passive margin domain on Syros (12SR18b). Intersecting colored lines indicate almandine (red), pyrope (green), grossular (blue) and spessartine (orange) isopleths. Garnet model abundance contours are shaded in green.

Lu/Hf system in garnet (Scherer et al., 2000), allowing interpretation of measured ages as crystallization ages. For all models, the trajectory between the isopleth intersections for garnet core to rim growth describes a phase of near-isobaric heating (Fig. 9b). Additionally, garnet modal abundance contours as modelled for matrix compositions show a further increase for P-T conditions that exceed the rim isopleth intersections, beyond garnet modes as observed in thin section (Fig. 7, 8). Thus, garnet growth in the samples was limited by maximum experienced P-T conditions, instead of by elemental budget constraints. As further subduction would have facilitated additional garnet growth, our recorded core to rim ages are interpreted to reflect cessation of subduction and

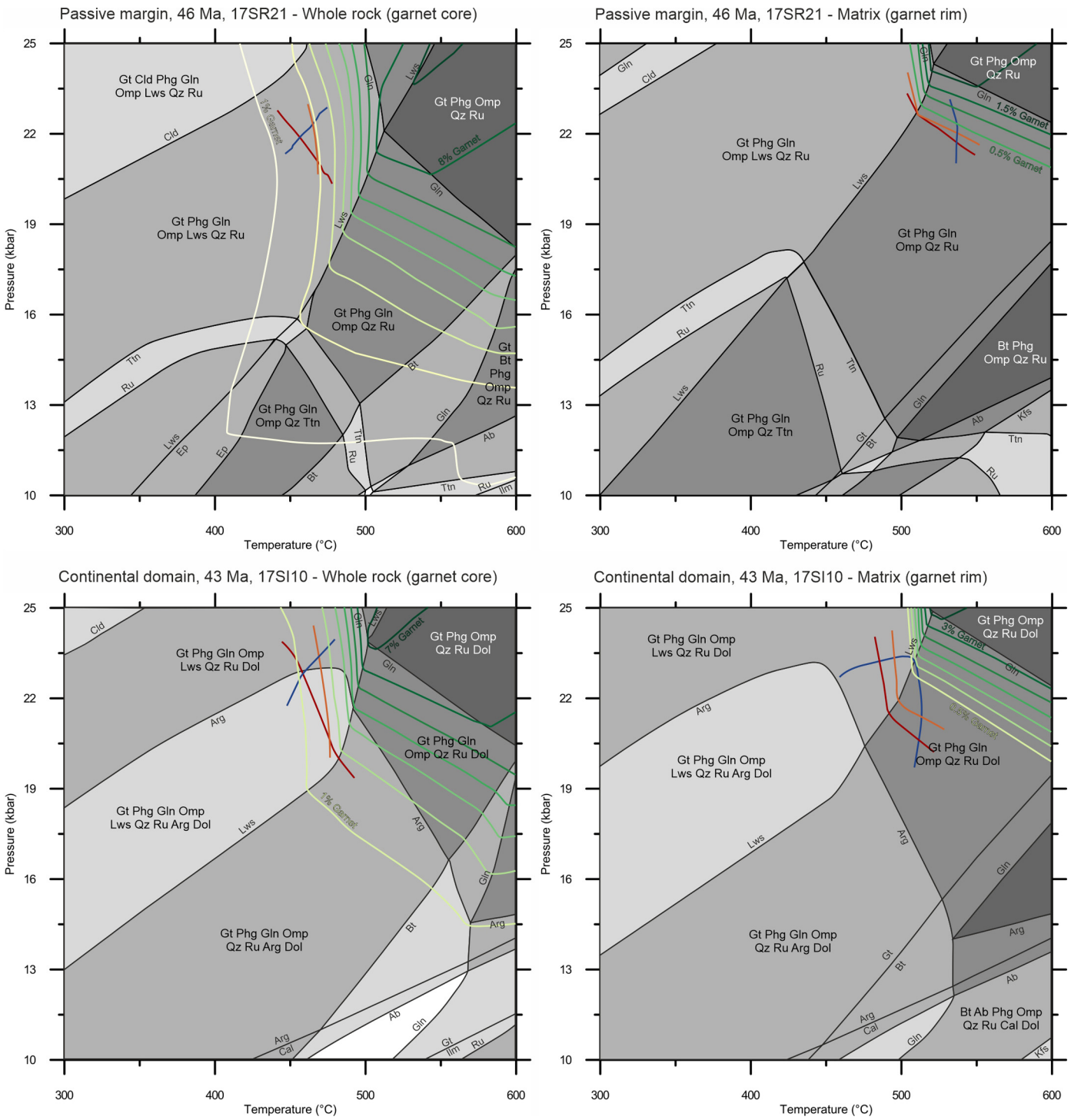

Fig. 8. Pseudosections for samples 17SR21 and 17SI10. Models for whole rock and matrix compositions reflect respective garnet core and rim growth for the lower passive margin domain on Syros (17SR21) and the continental domain on Sifnos (17SI10). Intersecting colored lines indicate almandine (red), pyrope (green), grossular (blue) and spessartine (orange) isopleths. Garnet model abundance contours are shaded in green.

the onset of exhumation for their hosting rocks. Polycyclic garnet growth has been described for some samples from these islands (Dragovic et al., 2015; Gorce et al., 2021) and may provide an alternative explanation for the apparent age trend. If enriched in Lu, younger garnet growth rims can progressively reduce the ages for the downward increasingly overprinted sequence. However, garnet with a documented polycyclic growth history has clear complex zoning patterns (Dragovic et al., 2015; Gorce et al., 2021), while our samples describe comparatively simple zoning trends (Fig. 5, except SY17-30). Therefore, the garnet ages are interpreted to reflect maximum burial and the onset of exhumation for their hosting subunit.

6.2. Imbricated supracrustal slices in the Cyclades

Our age data show that the distinct domains in the CBU on Syros and Sifnos record the Eocene transition from oceanic to continental subduction and exhumation. Sequential subduction affected oceanic rocks that reached maximum depths at ~ 52 Ma, a continental shelf that reached maximum pressures at ~ 48.5 Ma

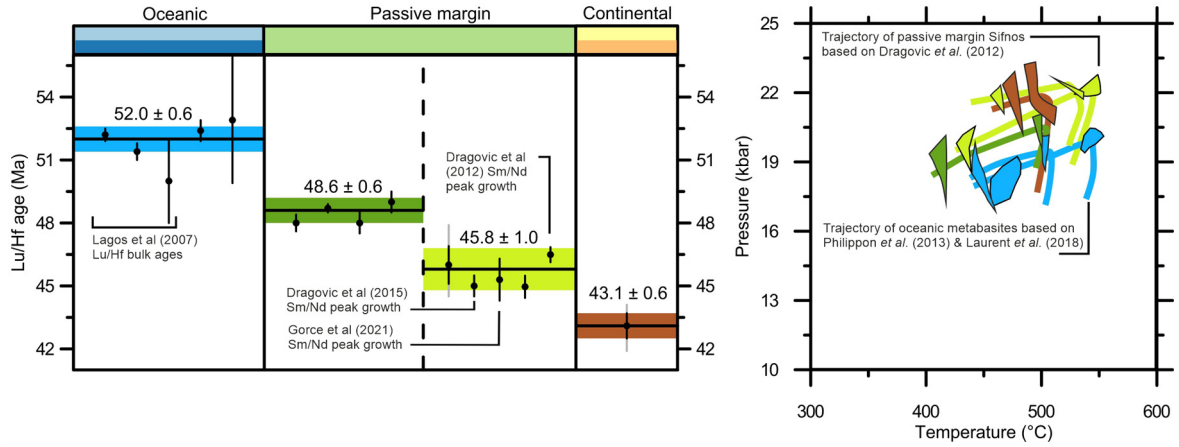

Fig. 9. Compilation of available garnet petrochronology data from Syros and Sifnos. a) Lu/Hf and Sm/Nd garnet-whole rock isochron ages compiled per tectonic domain and age group. Weighted average ages are presented with 2sd. Grey error bars based on isochrons using reproducibility of the internal standard (see section 4.2). b) Isopleth intersection fields and P-T conditions for garnet core and rim growth, reflecting maximum burial conditions. Trajectories are based on our own modelling results unless indicated otherwise.

and ~ 46 Ma, and continental rocks that started exhumation at ~ 43 Ma. While crustal material enters subduction zones continuously at 2–8 cm/yr, the garnet petrochronology seems to record episodic triggering of exhumation at 2–4 Myr intervals. While our sample set may have overlooked a more continuous age record in the sequence, the consistency of the ~ 46 and ~ 48.5 Ma age groups for passive margin sequences on two islands ~ 50 km apart suggests that exhumation was triggered synchronously at larger scales. The systematically downward increasing Lu/Hf age trend indicates that despite intense internal deformation, these rock fragments have retained some degree of internal coherence during exhumation. All these observations would fit models of exhumation as larger, coherent units (Chemenda et al., 1996) rather than models for exhumation as a chaotic melange (Shreve and Cloos, 1986). The dominance of supracrustal metasediments on the islands (Figs. 2–4) suggests detachment occurred relatively close to the slab surface, indicating only the top few kilometers of crustal rocks were detached and exhumed. This indicates that during the transition of oceanic to continental subduction, lower crust was initially still subducting.

Our data provide clear evidence for studies that have proposed peak metamorphic heterogeneity in the CBU (Avigad, 1993; Forster and Lister, 2005; Glodny and Ring, 2021). Asynchronous peak metamorphism implies that post-peak P-T-t evolution has also differed until the subunits were juxtaposed. The observed jumps in preserved metamorphic preservation suggest juxtaposition of the sequence is post-metamorphic, perhaps as late as during Miocene extension. Heterogeneous retrograde metamorphic conditions were previously proposed to explain the inverted gradient in recorded metamorphic overprint (Avigad, 1993; Trotet et al., 2001), in $^{40}Ar/^{39}Ar$ ages (Uunk et al., 2018) and in Rb/Sr ages (Glodny and Ring, 2021). Trends in overprint, $^{40}Ar/^{39}Ar$ and Rb/Sr ages have also been interpreted to be the effect of selective fluid infiltration during exhumation (Bröcker et al., 2013; Cliff et al., 2016), which may be at play at smaller scales within the exhumed units. At larger scale, the robust garnet Lu/Hf and Sm/Nd data confirm the more carefully interpreted phengite based $^{40}Ar/^{39}Ar$ and Rb/Sr age trends, validating the applicability of all three methods.

7. Consistent exhumation from a fixed depth

7.1. The conditions for detachment and exhumation

The uniformity of peak burial conditions for the different domains at 2–4 Myr age intervals (Fig. 9b) indicates exhumation was repeatedly triggered at a consistent depth in the subduction zone. If recovery of these supracrustal rocks can be related to a specific process or property of the subduction zone, this may provide new insights into the conditions determining whether crustal material is subducted in the mantle or exhumed to the surface. Rock detachment can be simplified to occur when positive buoyancy forces subjected on rocks exceed the strength of their coupling to the subducting plate (Chopin et al., 1987). When this condition is met, rocks may detach from the subducting plate and start to exhume. Mechanisms that trigger exhumation should then reflect processes that either increase subducting rock buoyancy or decrease their plate coupling strength.

Specific tectonic regimes such as slab rollback or indenter subduction may provide additional boundary conditions for rock exhumation (Brun and Faccenna, 2008; Vanderhaeghe and Duchêne, 2010; Warren, 2013), favoring exhumation by changing the subduction channel geometry or by supplying buoyant continental crust. However, these processes do not provide a relationship to a specific rock recovery depth and the recurrent nature of the exhumation excludes incidental processes as depth controlling mechanisms. Instead, the consistent recovery depth should be related to steady-state processes that modify the balance between positive buoyancy and mechanical strength at depth.

Positive buoyancy forces result from the density contrast between subducting rocks and the neighboring lower crust (2.7–3.1 g/cm^3) or mantle wedge (3.3–3.4 g/cm^3; Cloos, 1993). Densities for typical subducting passive margin and continental sediments range 2.7–3.1 g/cm^3 when metamorphosed in blueschist to eclogite facies (Hacker et al., 2011), providing positive buoyancy when juxtaposed against the denser mantle wedge. Mafic oceanic crust achieves higher densities of up to 3.5 g/cm^3 during high pressure metamorphism. However, bulk densities for oceanic rock units may be sufficiently low when they include serpentinites (2.6 g/cm^3; Guillot et al., 2001) or metasediments (2.7–3.1 g/cm^3).

Plate coupling strength is controlled by the internal strength of the subducting rocks. The plate coupling strength may vary strongly depending on material properties, as well as on the depth along the subduction interface (Agard et al., 2018). Previous authors have linked clusters in recovery depth for global data compiled for exhumed oceanic rocks to a decrease in mechanical strength resulting from specific mineral dehydration reactions or transitions in visco-elastic behavior (Agard et al., 2018). A recovery depth cluster near ~30 km has been related to a brittle-ductile transition for phyllosilicates, while a cluster near ~ 80 km

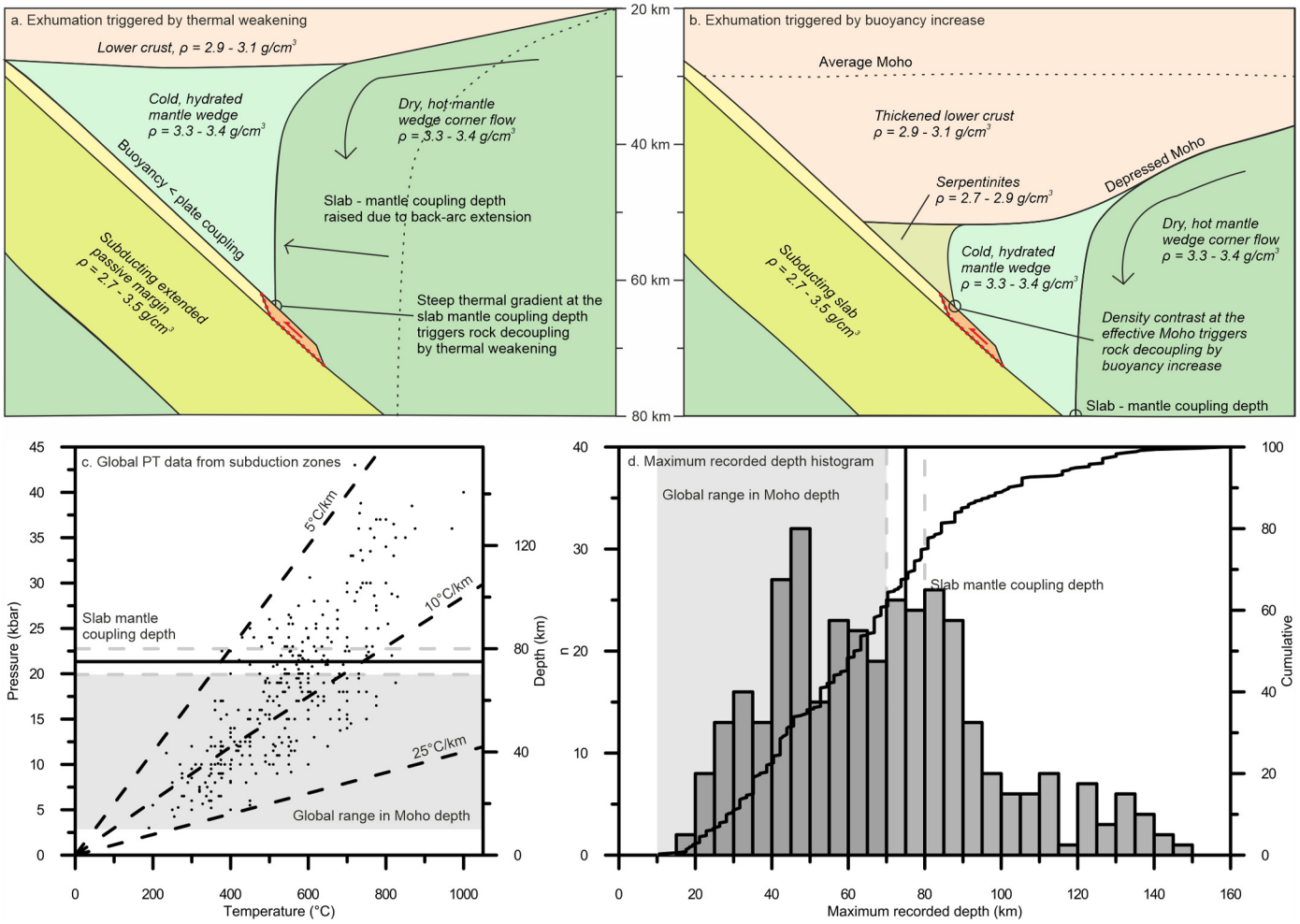

Fig. 10. a, b) Theoretical models for consistent exhumation triggered at 65–70 km depth within a subduction zone. a) Exhumation for strongly coupled rocks triggered by thermal weakening at the slab mantle decoupling depth, which is raised due to back-arc extension in the overriding plate. b) Exhumation for weakly coupled rocks by buoyancy increase at the crust-mantle boundary, which is depressed by crustal thickening in the overriding plate. c) Compiled global P-T data for subduction zones, from Penniston-Dorland et al. (2015). d) Histogram and cumulative values for depth converted from pressure of Fig. 3. Grey box in c and d indicates the range in global Moho depth, the full and dashed lines indicate the position of the slab mantle coupling depth ±5 km.

is related to destabilization of serpentinite. A third cluster near 55–60 km depth is related to water release from breakdown of minerals like chlorite and lawsonite (Agard et al., 2018). However, these processes relate to these specific oceanic rock types and P-T conditions of metamorphic reactions are strongly lithologically controlled. Importantly, we observe similar maximum burial depths for rocks of oceanic, passive margin and continental provenance (Fig. 9b), which yield contrasting lithologies and material properties (Figs. 2–4). Therefore, the consistent depth window observed here seems to be unrelated to the strongly varying properties of the subducting material. Instead, we explore steady-state properties of subduction zones as possible mechanisms to trigger exhumation by modifying the balance between rock buoyancy and mechanical strength.

7.2. Mechanisms for consistent rock recovery

For average crust and mantle densities of 2.85 and 3.3 g/cm^3 respectively, pressures of ∼ 20 kbar provide a depth of 65–70 km at which the exhumation trigger has operated. At this depth, we consider thermal weakening at the slab-mantle coupling depth (Fig. 10a) or buoyancy increase at the crust-mantle boundary (Fig. 10b) as potential triggers for consistent exhumation of subducting supracrustal rocks.

7.2.1. Thermal weakening at the slab-mantle coupling depth?

Based on heat flow modelling of modern oceanic subduction zones, a coupling is proposed to occur at 75 ± 5 km depth between the downgoing plate and mantle wedge corner flow (Wada and Wang, 2009). This depth may act as a 'point of no return' for subducting rocks, as rock detachment is less likely when mechanical coupling is achieved between corner flow and the subducting slab (Whitney et al., 2014) and eclogitisation provides a negative buoyancy for subducting mafic rocks (Agard et al., 2018). Before this coupling point, the mantle wedge is assumed to be cold and partially serpentinized due to subduction hydration. After this point, the mantle wedge is dry due to serpentinite destabilization and incoming mantle wedge corner flow results in a steep thermal gradient (Wada and Wang, 2009). The coupling depth has been suggested to trigger exhumation (Aygül and Oberhänsli, 2017; Bayet et al., 2018), as the steep temperature gradient may decrease mechanical strength sufficiently to be overcome by the positive buoyancy for subducting supracrustal rocks (Fig. 10a).

For this model to account for consistent exhumation in the Cyclades, the coupling depth must have been raised from the proposed 70–80 km (Wada and Wang, 2009) to the recorded recovery depth for the exhumed rocks in this study of 65–70 km. It has been suggested that back-arc extension may raise the slab mantle coupling depth (Aygül and Oberhänsli, 2017), which for the Hellenic subduction system would fit with Eocene core-complex

type extension as recorded in the Rhodopes (Brun and Sokoutis, 2018). Additionally, this model would fit with the phase of isobaric heating as modelled for our samples (Fig. 9b). However, for these supracrustal rocks to be subducted into the mantle, their initial plate coupling strength would have to be greater than their positive buoyancy in the mantle (Fig. 10a).

7.2.2. The Moho as a subduction barrier?

If rocks are weakly coupled to the subducting plate, exhumation can be triggered as soon as positive buoyancy is increased (Fig. 10b). Buoyancy for subducting supracrustal rocks may show a stepped increase due to an increase in ambient density at the crust-mantle boundary of the upper plate, or the Moho. Supracrustal metamorphic sequences as observed on Syros and Sifnos may contain abundant weak potential detachment horizons, including mica-rich lithologies, marbles, serpentinites, pre-existing shear zones or lithological boundaries. Therefore, it may be likely that plate coupling strength for supracrustal rocks is not strong enough to withstand a stepped increase in rock buoyancy at the Moho (Fig. 10b). The depth of consistent triggering of exhumation would then be directly linked to the position of the upper plate Moho, which acts as a subduction barrier for weak supracrustal rocks.

Relating the observed recovery depth of 65–70 km to the Moho would require a considerably depressed Moho of $\sim$ 60 km as compare to the average continental crustal Moho of $\sim$ 30 km. A thickened overriding plate for the Hellenic subduction zone would fit Late Cretaceous collision of the Pelagonian-Lycian block with remnants of the Vardar ocean and Rhodopes, before Neogene extension (van Hinsbergen et al., 2005). Significant hydration of the mantle wedge to low density serpentinite could also further increase the depth at which the buoyancy increase is experienced by rocks in the downgoing plate (Fig. 10b). While the validity of either model depends on the geometry of the Hellenic subduction zone during the Eocene and the mechanical strength of supracrustal rocks in the downgoing plate, they both provide potential mechanisms to explain the observed systematic triggering of exhumation from a fixed depth.

7.3. Global perspective

The increased spatial resolution for our dataset, covering units with varying provenance and material properties, permits an interpretation relating rock recovery to subduction zone properties. Recent high resolution studies on the Sesia Zone (Giuntoli et al., 2018) and the Tian Shan (Bayet et al., 2018) similarly describe consistent maximum burial depths for sequentially subducted units, indicating episodic recovery from a fixed depth may be a more common phenomenon. In the global record, compiled data for exhumed rocks define a range in maximum recorded pressure of 5–45 kbar (Fig. 10c; Penniston-Dorland et al., 2015). Conversion of pressure to depth allows an interpretation of the depth distribution (Fig. 10d). About $\sim$ 80% of the data points cover the range of global Moho depths of 30–75 km and the inferred slab mantle coupling point at 75 km, suggesting a potential relationship to these subduction parameters. Similarly, it is likely that that recovery depth clusters of $\sim$ 30, $\sim$ 50–60 and $\sim$ 80 km as observed for compiled oceanic rocks (Agard et al., 2018) may in part also reflect subduction zone properties rather than material properties.

Like in our study area, exhumed oceanic rocks are commonly found in association with continental fragments and in former accretionary or collisional subduction settings (e.g. most alpine belts in Table 2 of Agard et al., 2018). This indicates that the occurrence of exhumation for oceanic and continental crust is essentially similar and the mechanisms for their detachment from the subducting plate may be similar too. At larger spatial and temporal scales, the Cyclades also record lower maximum burial depths for subducted and exhumed units (Glodny and Ring, 2021; Grasemann et al., 2017). While our data reveals systematic exhumation at intervals of $\sim$ 2–4 Myr for $\sim$ 10 Myr at the scale of islands, spatial and temporal differences in rock recovery behavior at orogenic scales may be related to along strike differences in subduction zone geometry and kinematic changes in plate boundaries (Brun and Faccenna, 2008; Hacker and Gerya, 2013; Vanderhaeghe and Duchêne, 2010; Warren, 2013).

8. Conclusions

We subdivide the sequences on Syros and Sifnos islands into domains of interpreted oceanic, passive margin and continental provenance. We show that the sequence shows a stepped downward decrease for garnet growth ages, averaging 52 ± 0.6 Ma for the oceanic domain, 48.6 ± 0.6 and 45.8 ± 1.0 Ma for the passive margin domain and 43.1 ± 0.6 Ma for the continental domain. Garnets from all age groups were modelled to have grown during a phase of isobaric heating from 400 °C to 550 °C in a narrow pressure range of 19–21 kbar. Our data are the first to show age differences for peak metamorphism at the island scale. We show the islands consist of imbricated supracrustal subunits that retained some degree of coherence during exhumation in the subduction channel. The similar maximum burial conditions recorded at 2–4 Myr intervals for rocks of different provenance indicate that the highly variable material properties have not resulted in a different recovery depth. Instead, we relate the consistent exhumation from a fixed depth to steady-state properties of the subduction zone. We propose that the slab mantle coupling depth or the crust mantle boundary may trigger exhumation by weakening of the subducting material or by increasing rock buoyancy, respectively. Depending on subduction channel geometry and the strength of subducting rocks, these processes could facilitaite rock recovery in the range of 30–80 km depth, which overlap the majority of maximum recorded burial conditions worldwide.

CRediT authorship contribution statement

The following contributions to the paper have led to our decisions for co-authorship. B.U. lead the study, conducted field work and collected 5 of the dated samples, conducted EPMA and XRF analysis for 2 of the samples which were used for modelling, conducted mineral separation and chemical procedures for Lu/Hf dating, conducted thermodynamic modelling and wrote the manuscript. F.B. participated in field work, contributed to thermodynamic modelling, contributed to the rationale of the study and participated in writing the manuscript. M.d.P.A. participated in field work, collected four of the dated samples, conducted XRF and EPMA analysis for those samples and contributed to the manuscript. R.H. participated in field work, conducted EPMA and XRF analysis for four samples, two of which were used for thermodynamic modelling. K.v.Z. conducted Lu/Hf isotopic analysis. R.v.t.V. contributed to thermodynamic modelling and to discussion on the mechanism for steady state exhumation. J.W. supervised both the field aspect and the interpretation of results, and contributed to writing of the manuscript.

Declaration of competing interest

The authors declare that they have no known competing financial interests or personal relationships that could have appeared to influence the work reported in this paper.

Acknowledgements

This manuscript benefited from reviews of earlier versions by Konstanze Stübner, Laurent Jolivet, Andrew Kylander-Clark, Besim Dragovic, Olivier Vanderhaeghe and several anonymous reviewers.

Appendix A. Supplementary material

Supplementary material related to this article can be found online at https://doi.org/10.1016/j.epsl.2022.117479.

References

Agard, P., Plunder, A., Angiboust, S., Bonnet, G., Ruh, J., 2018. The subduction plate interface: rock record and mechanical coupling (from long to short timescales). Lithos 320–321, 537–566.

Aravadinou, E., Xypolias, P., Chatzaras, V., Iliopoulos, I., Gerogiannis, N., 2015. Ductile nappe stacking and refolding in the Cycladic Blueschist Unit: insights from Sifnos Island (south Aegean Sea). Int. J. Earth Sci., 1–22.

Avigad, D., 1993. Tectonic juxtaposition of blueschists and greenschists in Sifnos Island (Aegean Sea) – implications for the structure of the Cycladic blueschist belt. J. Struct. Geol. 15, 1459–1469.

Aygül, M., Oberhänsli, R., 2017. Tectonic stacking of HP/LT metamorphic rocks in accretionary wedges and the role of shallowing slab-mantle decoupling. Tectonics 36, 2332–2346.

Bayet, L., John, T., Agard, P., Gao, J., Li, J.-L., 2018. Massive sediment accretion at ~ 80 km depth along the subduction interface: evidence from the southern Chinese Tianshan. Geology 46, 495–498.

Brady, J.B., Markley, M.J., Schumacher, J.C., Cheney, J.T., Bianciardi, G.A., 2004. Aragonite pseudomorphs in high-pressure marbles of Syros, Greece. J. Struct. Geol. 26, 3–9.

Bröcker, M., Baldwin, S., Arkudas, R., 2013. The geological significance of 40Ar/39Ar and Rb–Sr white mica ages from Syros and Sifnos, Greece: a record of continuous (re)crystallization during exhumation? J. Metamorph. Geol. 31, 629–646.

Brun, J.-P., Faccenna, C., 2008. Exhumation of high-pressure rocks driven by slab rollback. Earth Planet. Sci. Lett. 272, 1–7.

Brun, J.-P., Sokoutis, D., 2018. Core complex segmentation in North Aegean, a dynamic view. Tectonics 37, 1797–1830.

Chemenda, A.I., Mattauer, M., Bokun, A.N., 1996. Continental subduction and a mechanism for exhumation of high-pressure metamorphic rocks: new modelling and field data from Oman. Earth Planet. Sci. Lett. 143, 173–182.

Chopin, C., Gibbons, W., Platt, J.P., Artyushkov, E.V., Oxburgh, E.R., Yardley, B.W.D., England, P.C., 1987. Very-high-pressure metamorphism in the western Alps: implications for subduction of continental crust. Philos. Trans. R. Soc. Lond. Ser. A, Math. Phys. Sci. 321, 183–197.

Cliff, R.A., Bond, C.E., Butler, R.W.H., Dixon, J.E., 2016. Geochronological challenges posed by continuously developing tectonometamorphic systems; insights from Rb–Sr mica ages from the Cycladic Blueschist Belt, Syros (Greece). J. Metamorph. Geol. 35, 197–211.

Cloos, M., 1993. Lithospheric buoyancy and collisional orogenesis: subduction of oceanic plateaus, continental margins, island arcs, spreading ridges, and seamounts. Geol. Soc. Am. Bull. 105, 715–737.

Connolly, J.A.D., 2009. The geodynamic equation of state: what and how. Geochem. Geophys. Geosyst. 10.

Diener, J.F.A., Powell, R., 2012. Revised activity–composition models for clinopyroxene and amphibole. J. Metamorph. Geol. 30, 131–142.

Dragovic, B., Baxter, E.F., Caddick, M.J., 2015. Pulsed dehydration and garnet growth during subduction revealed by zoned garnet geochronology and thermodynamic modeling, Sifnos, Greece. Earth Planet. Sci. Lett. 413, 111–122.

Dragovic, B., Samanta, L.M., Baxter, E.F., Selverstone, J., 2012. Using garnet to constrain the duration and rate of water-releasing metamorphic reactions during subduction: an example from Sifnos, Greece. Chem. Geol. 314–317, 9–22.

Ernst, W.G., Maruyama, S., Wallis, S., 1997. Buoyancy-driven, rapid exhumation of ultrahigh-pressure metamorphosed continental crust. Proc. Natl. Acad. Sci. USA 94, 9532–9537.

Forster, M.A., Lister, G.S., 2005. Several distinct tectono-metamorphic slices in the Cycladic eclogite–blueschist belt, Greece. Contrib. Mineral. Petrol. 150, 523–545.

Fuhrman, M.L., Lindsley, D.H., 1988. Ternary-feldspar modeling and thermometry. Am. Mineral. 73, 201–215.

Gerya, T.V., Stöckhert, B., Perchuk, A.L., 2002. Exhumation of high-pressure metamorphic rocks in a subduction channel: a numerical simulation. Tectonics 21, 6-1–6-19.

Giuntoli, F., Lanari, P., Burn, M., Kunz, B.E., Engi, M., 2018. Deeply subducted continental fragments – Part 2: insight from petrochronology in the central Sesia Zone (western Italian Alps). Solid Earth 9, 191–222.

Glodny, J., Ring, U., 2021. The Cycladic Blueschist Unit of the Hellenic subduction orogen: protracted high-pressure metamorphism, decompression and reimbrication of a diachronous nappe stack. Earth-Sci. Rev. 103883.

Gorce, J.S., Caddick, M.J., Baxter, E.F., Dragovic, B., Schumacher, J.C., Bodnar, R.J., Kendall, J.F., 2021. Insight into the early exhumation of the Cycladic Blueschist Unit, Syros, Greece: combined application of zoned garnet geochronology, thermodynamic modeling, and quartz elastic barometry. Geochem. Geophys. Geosyst. 22, e2021GC009716.

Grasemann, B., Huet, B., Schneider, D.A., Rice, A.H.N., Lemonnier, N., Tschegg, C., 2017. Miocene postorogenic extension of the Eocene synorogenic imbricated Hellenic subduction channel: new constraints from Milos (Cyclades, Greece). Geol. Soc. Am. Bull. 130, 238–262.

Green, E., Holland, T., Powell, R., 2007. An order-disorder model for omphacitic pyroxenes in the system jadeite-diopside-hedenbergite-acmite, with applications to eclogitic rocks. Am. Mineral. 92, 1181–1189.

Guillot, S., Hattori, K.H., de Sigoyer, J., Nägler, T., Auzende, A.-L., 2001. Evidence of hydration of the mantle wedge and its role in the exhumation of eclogites. Earth Planet. Sci. Lett. 193, 115–127.

Hacker, B.R., Gerya, T.V., 2013. Paradigms, new and old, for ultrahigh-pressure tectonism. Tectonophysics 603, 79–88.

Hacker, B.R., Kelemen, P.B., Behn, M.D., 2011. Differentiation of the continental crust by relamination. Earth Planet. Sci. Lett. 307, 501–516.

Hamelin, C., Brady, J.B., Cheney, J.T., Schumacher, J.C., Able, L.M., Sperry, A.J., 2018. Pseudomorphs after Lawsonite from Syros, Greece. J. Petrol. 59, 2353–2384.

Holland, T.J.B., Powell, R., 1998. An internally consistent thermodynamic data set for phases of petrological interest. J. Metamorph. Geol. 16, 309–343.

Keiter, M., Ballhaus, C., Tomaschek, F., 2011. A New Geological Map of the Island of Syros (Aegean Sea, Greece): Implications for Lithostratigraphy and Structural History of the Cycladic Blueschist Unit. Geological Society of America.

Lagos, M., Scherer, E.E., Tomaschek, F., Münker, C., Keiter, M., Berndt, J., Ballhaus, C., 2007. High precision Lu–Hf geochronology of Eocene eclogite-facies rocks from Syros, Cyclades, Greece. Chem. Geol. 243, 16–35.

Lamont, T.N., Searle, M.P., Waters, D.J., Roberts, N.M.W., Palin, R.M., Smye, A., Dyck, B., Gopon, P., Weller, O.M., St-Onge, M.R., 2019. Compressional origin of the Naxos metamorphic core complex, Greece: structure, petrography, and thermobarometry. Geol. Soc. Am. Bull. 132, 149–197.

Laurent, V., Jolivet, L., Roche, V., Augier, R., Scaillet, S., Cardello, G.L., 2016. Strain localization in a fossilized subduction channel: insights from the Cycladic Blueschist Unit (Syros, Greece). Tectonophysics 672–673, 150–169.

Laurent, V., Lanari, P., Naïr, I., Augier, R., Lahfid, A., Jolivet, L., 2018. Exhumation of eclogite and blueschist (Cyclades, Greece): pressure–temperature evolution determined by thermobarometry and garnet equilibrium modelling. J. Metamorph. Geol. 36, 769–798.

Münker, C., Weyer, S., Scherer, E., Mezger, K., 2001. Separation of high field strength elements (Nb, Ta, Zr, Hf) and Lu from rock samples for MC-ICPMS measurements. Geochem. Geophys. Geosyst. 2.

Pe-Piper, G., 1998. The nature of Triassic extension-related magmatism in Greece: evidence from Nd and Pb isotope geochemistry. Geol. Mag. 135, 331–348.

Penniston-Dorland, S.C., Kohn, M.J., Manning, C.E., 2015. The global range of subduction zone thermal structures from exhumed blueschists and eclogites: rocks are hotter than models. Earth Planet. Sci. Lett. 428, 243–254.

Philippon, M., Brun, J.P., Gueydan, F., 2011. Tectonics of the Syros blueschists (Cyclades, Greece): from subduction to Aegean extension. Tectonics 30, TC4001.

Philippon, M., Gueydan, F., Pitra, P., Brun, J.P., 2013. Preservation of subduction-related prograde deformation in lawsonite pseudomorph-bearing rocks. J. Metamorph. Geol. 31, 571–583.

Platt, J.P., 1986. Dynamics of orogenic wedges and the uplift of high-pressure metamorphic rocks. Geol. Soc. Am. Bull. 97, 1037–1053.

Ring, U., Pantazides, H., Glodny, J., Skelton, A., 2020. Forced return flow deep in the subduction channel, Syros, Greece. Tectonics 39, e2019TC005768.

Roche, V., Laurent, V., Cardello, G.L., Jolivet, L., Scaillet, S., 2016. Anatomy of the Cycladic Blueschist Unit on Sifnos Island (Cyclades, Greece). J. Geodyn. 97, 62–87.

Scherer, E.E., Cameron, K.L., Blichert-Toft, J., 2000. Lu–hf garnet geochronology: closure temperature relative to the Sm–Nd system and the effects of trace mineral inclusions. Geochim. Cosmochim. Acta 64, 3413–3432.

Schumacher, J.C., Brady, J.B., Cheney, J.T., Tonnsen, R.R., 2008. Glaucophane-bearing marbles on Syros, Greece. J. Petrol. 49, 1667–1686.

Seck, H.A., 1996. Geochemistry of a meta-ophiolite suite: an association of metagabbros, eclogites and glaucophanites on the island of Syros, Greece. Eur. J. Mineral. 8, 607–624.

Shreve, R.L., Cloos, M., 1986. Dynamics of sediment subduction, melange formation, and prism accretion. J. Geophys. Res., Solid Earth 91, 10229–10245.

Smye, A.J., Greenwood, L.V., Holland, T.J.B., 2010. Garnet–chloritoid–kyanite assemblages: eclogite facies indicators of subduction constraints in orogenic belts. J. Metamorph. Geol. 28, 753–768.

Tracy, R.J., Robinson, P., Thompson, A.B., 1976. Garnet composition and zoning in the determination of temperature and pressure of metamorphism, central Massachusetts. Am. Mineral. 61, 762–775.

Trotet, F., Vidal, O., Jolivet, L., 2001. Exhumation of Syros and Sifnos metamorphic rocks (Cyclades, Greece). New constraints on the P-T paths. Eur. J. Mineral. 13, 901–920.

Uunk, B., Brouwer, F., ter Voorde, M., Wijbrans, J., 2018. Understanding phengite argon closure using single grain fusion age distributions in the Cycladic Blueschist Unit on Syros, Greece. Earth Planet. Sci. Lett. 484, 192–203.

van Hinsbergen, D.J.J., Hafkenscheid, E., Spakman, W., Meulenkamp, J.E., Wortel, R., 2005. Nappe stacking resulting from subduction of oceanic and continental lithosphere below Greece. Geology 33, 325–328.
Vanderhaeghe, O., Duchêne, S., 2010. Crustal-scale mass transfer, geotherm and topography at convergent plate boundaries. Terra Nova 22, 315–323.
Vervoort, J.D., Patchett, P.J., Söderlund, U., Baker, M., 2004. Isotopic composition of Yb and the determination of Lu concentrations and Lu/Hf ratios by isotope dilution using MC-ICPMS. Geochem. Geophys. Geosyst. 5.
Wada, I., Wang, K., 2009. Common depth of slab-mantle decoupling: reconciling diversity and uniformity of subduction zones. Geochem. Geophys. Geosyst. 10.
Warren, C.J., 2013. Exhumation of (ultra-)high-pressure terranes: concepts and mechanisms. Solid Earth 4, 75–92.
Warren, C.J., Beaumont, C., Jamieson, R.A., 2008. Modelling tectonic styles and ultra-high pressure (UHP) rock exhumation during the transition from oceanic subduction to continental collision. Earth Planet. Sci. Lett. 267, 129–145.
White, R.W., Powell, R., Holland, T.J.B., Johnson, T.E., Green, E.C.R., 2014. New mineral activity–composition relations for thermodynamic calculations in metapelitic systems. J. Metamorph. Geol. 32, 261–286.
Whitney, D.L., Teyssier, C., Seaton, N.C.A., Fornash, K.F., 2014. Petrofabrics of high-pressure rocks exhumed at the slab-mantle interface from the “point of no return” in a subduction zone (Sivrihisar, Turkey). Tectonics 33, 2315–2341.